ChemElectroChem

Research Article
doi.org/10.1002/celc.202300505

Chemistry Europe
European Chemical Societies Publishing

www.chemelectrochem.org

Impacts of Graphene Nanoribbon Production Methods on Oxygen-Reduction Electrocatalysis in Different Environments

Eduardo S. F. Cardoso,[a, b] Guilherme V. Fortunato,*[b, c] Clauber D. Rodrigues,[d] Fausto E. B Júnior,[b] Marc Ledendecker,[c] Marcos R. V. Lanza,[b] and Gilberto Maia*[a]

Graphene-based materials have emerged as highly promising catalysts for enhancing oxygen reduction reaction (ORR), a pivotal process in diverse energy conversion applications and the production of eco-friendly oxidants like hydrogen peroxide (H_2O_2). To design exceptionally efficient catalysts tailored to specific applications, it is essentially crucial to have a thorough understanding of their electrocatalytic behaviour. This involves ascribing functions to structural characteristics like defects and exploring heteroatom doping in graphene matrices. In this work, we study the synthesis of graphene nanoribbons (GNRs) derived from multi-walled carbon nanotubes (MWCNTs) and their doping with nitrogen (N) and phosphorus (P). We investigate how edge defects and oxygenated groups retained from the MWCNT opening process impact both the doping process and GNR electrocatalytic characteristics, with a focus on their relevance to ORR. Our findings underscore the need to optimize GNR structures and doping strategies for specific reaction conditions. We demonstrate how GNR characteristics are effectively influenced by varying MWCNT opening methods, ultimately affecting ORR performance and H_2O_2 selectivity. The findings show that when MWCNTs are opened to create GNRs with a broader distribution of oxygen atoms across the basal plane and fewer exposed edges, N-insertion enhances catalytic activity, resulting in improved ORR performance. However, this alteration reduces H_2O_2 selectivity in both acidic and alkaline media. On the other hand, generating GNRs with abundant edges and widespread oxygen functional groups on both the basal plane and edges yields a high oxygen group concentration. This configuration not only facilitates phosphorus insertion at the edges but also plays a crucial role in enhancing ORR performance, leading to selectivities of over 92% for H_2O_2 production in alkaline media. This study not only advances our understanding of graphene-based catalysts but also offers meaningful contributions and insights into the development of more efficient and sustainable electrochemical technologies in the realm of energy conversion.

Introduction

In recent years, graphene has emerged as a highly desirable carbon material with diverse, groundbreaking applications, and which has particularly become widely applied as a catalyst material in various energy conversion-related electrocatalytic processes.[1–5] When it comes to its suitability for application in catalysis, the key attributes of graphene lie in its valuable characteristics, which include typically high surface area, excellent conductivity, chemical inertness, and ease of functionalization tailored to specific catalytic processes.[1–3]

Graphene, which is known to be composed of a single layer of carbon atoms arranged in a crystalline lattice, can be synthesized from various carbon-containing precursors using a range of chemical and physical methods.[1,2,6–9] The application of this diverse array of synthesis possibilities results in the development of a myriad of materials with structural variations that lead to significant disparities in the physical and chemical properties of the synthesized materials. More recently, one of the key avenues of research in this field has involved the synthesis and exploration of graphene derived from carbon nanotubes (CNTs), which leads to the development of suitable carbonaceous materials with exceptional properties and intriguing opportunities for functionalization due to their nanoribbon-like structure.[6,10–13] Owing to their elongated strip-like configuration, graphene nanoribbons (GNR) can exhibit metallic or semiconductor features as a function of their width, edge structure, and the presence of functional groups.[1,2,6,14] In applications related to electrochemical energy conversion, it is known that

[a] Dr. E. S. F. Cardoso, Prof. Dr. G. Maia
Institute of Chemistry
Federal University of Mato Grosso do Sul
Av. Senador Filinto Muller 1555, Campo Grande, MS 79074–460 (Brazil)
E-mail: gilberto.maia@ufms.br

[b] Dr. E. S. F. Cardoso, Dr. G. V. Fortunato, F. E. B Júnior, Prof. Dr. M. R. V. Lanza
São Carlos Institute of Chemistry
University of São Paulo
Avenida Trabalhador São-Carlense 400, São Carlos, SP 13566–590 (Brazil)

[c] Dr. G. V. Fortunato, Prof. Dr. M. Ledendecker
Sustainable Energy Materials
Technical University Munich
Campus Straubing, Schulgasse 22, 94315 Straubing (Germany)
E-mail: g.fortunato@tum.de

[d] Dr. C. D. Rodrigues
State University of Mato Grosso do Sul
Rua Rogério Luis Rodrigues s/n, Glória de Dourados, MS 79730–000 (Brazil)

Supporting information for this article is available on the WWW under https://doi.org/10.1002/celc.202300505

the presence of defects as well as functional groups in graphene structures plays a pivotal role in the reaction process, especially in electrocatalytic reactions such as oxygen reduction reaction (ORR).[8,15–18]

ORR plays a crucial role in various applications, including fuel cell cathodes and the production of environmentally friendly oxidants like hydrogen peroxide (H_2O_2).[18–20] The catalytic activity, which reflects how readily the reaction occurs, along with the selectivity in generating either water or H_2O_2 as the primary reaction product, particularly in both acidic and alkaline environments (as shown in equations Eqs. 1–4),[19,21,22] serves as a fundamental determinant of the successful utilization of ORR. In specific contexts, the quest for the development of highly efficient electrode materials which selectively catalyze either of these reactions with minimal overpotential stands as a central objective in this research domain. Remarkably, graphene-based materials have emerged as highly promising candidates since their application in reaction catalysis helps facilitate energy production (with H_2O or OH^- as the primary product) or H_2O_2 (or HO_2^-) production via different media.[8,14–18,20,23,24]

$$O_2 + 4H^+ + 4e^- \rightarrow 2H_2O \ (\text{in acidic media}) \quad (1)$$

$$O_2 + 2H^+ + 2e^- \rightarrow H_2O_2 \ (\text{in acidic media}) \quad (2)$$

$$O_2 + 2H_2O + 4e^- \rightarrow 4OH^- \ (\text{in alkaline media}) \quad (3)$$

$$O_2 + H_2O + 2e^- \rightarrow HO_2^- + OH^- \ (\text{in alkaline media}) \quad (4)$$

To boost our understanding regarding the catalytic behaviour of graphene-based materials, one needs to consider the role played by defects in these materials. Defects in graphene structures give rise to heterogeneity in the electronic and chemical properties, which can significantly influence the electrocatalytic activity.[18,20,25] These defects may be either intrinsic in nature, such as vacancies or Stone-Wales defects, or extrinsic, such as edge defects that stem from the synthesis process.[6,26,27] In the context of ORR under the application of GNR-based catalysts, edges can serve as active sites for oxygen adsorption and facilitate the occurrence of subsequent reduction reactions.[8,28]

Functionalization via heteroatom doping is another critical way of modulating the catalytic properties of graphene. The controlled introduction of elements like nitrogen (N), oxygen (O), and phosphorus (P) into graphene lattice can provoke changes in its electronic structure.[5,14,20] N-doping, for instance, introduces additional electron-rich sites into the catalyst structure, and this enhances the electrocatalytic activity for ORR by changing the density charge of surrounding carbon atoms.[25,29] P-doping in graphene may provoke structural disruptions in the hexagonal arrangement of carbon atoms and charge imbalances due to the relatively larger covalent radius of phosphorus and its lower electronegativity compared to carbon and nitrogen.[30–32] Electrons can be repelled from the P atom due to its higher electron-donating ability, and this alters the electronic structure and reactivity of nearby carbon atoms, which, in turn, can influence how O_2 molecules interact with the graphene surface during ORR.[30–33] O-doping can lead to the incorporation of functional groups into the catalyst structure which also strongly affect the electronic structure and reactivity of neighbouring carbon atoms in the graphene matrix.[14,23–25,34,35] Furthermore, it is well-known that the presence of oxygen functional groups in carbon materials is crucial for promoting the selective production of H_2O_2.[24,36–38] More recently, we have shown that O-groups can also provide insertion points for replacement during doping with other heteroatoms.[14,23,39]

When it comes to synthesizing GNRs through top-down chemical oxidation methods involving multiwalled carbon nanotubes (MWCNTs), one can find a rich body of literature with well-documented reports and elucidations about the process.[6,8,10–13,40–44] These methods employ different conditions and a wide range of oxidizing agents, including H_2SO_4, $KMnO_4$, H_2SO_4-KNO_3, or combinations of these agents, to unzip MWCNTs and produce GNRs. It is worth noting that the synthesis method employed can exert a significant influence on the structural and electrocatalytic properties of GNRs – an aspect that has not yet been comprehensively explored within the context of ORR. For illustration purposes, the method proposed by Tour *et al.*[6] and the approach developed by our research group[8] each present unique advantages and disadvantages regarding scalability, yield and, above all, in relation to the differences in structural characteristics of the GNRs produced, which is a key point to consider when it comes to the successful application of these carbon materials. Thus, boosting our understanding on how doping and defects impact the catalytic activity and selectivity of GNRs in ORR has the potential to help us widen their application, particularly within the realm of energy conversion technologies. This knowledge can pave the way for the development of more informed and tailored approaches toward the conduct of electrocatalytic processes that will help us harness the full potential of GNRs in terms of enhancing these processes.

In this article, we present a comprehensive investigation into the synthesis of GNRs via top-down chemical oxidation of MWCNTs, and their subsequent doping with nitrogen (N) and phosphorus (P). The central objective is to broaden our understanding on how edge defects and oxygenated groups, retained from the MWCNT opening process, influence both the doping process and the electrocatalytic characteristics of GNRs, with a specific focus on their relevance in ORR. The present study provides significant contributions to researchers in the field for two primary reasons. Firstly, through a rigorous comparative analysis of the method proposed by Tour *et al.* and our proposed method, we have successfully produced a range of GNR matrices with comparable edge defects and oxygenated groups and subjected them to rigorous evaluation. Secondly, by using a soft doping procedure with minimal impact on the synthesized GNR matrices, we thoroughly explore the physical-chemical properties of these GNR matrices, where we shed light on their suitability for efficient functionalization, as well as their consequential effects on ORR activity and selectivity within acidic and alkaline environments. Our overarching goal is to help shed light on the synthesis strategies that lead to the development of functionalized GNRs with optimal catalytic properties for ORR. The findings of this study will help improve our understanding of graphene-

based catalysts and provide meaningful contributions and insights into the development of more efficient and sustainable electrochemical technologies.

Through a combination of comprehensive physical-chemical material characterization and an extensive ORR study employing a rotating ring-disk electrode setup (RRDE), we demonstrate that in an acidic medium, undoped GNRs with higher oxygen content and increased edge defects produce more H_2O_2. N-doping, which reduces oxygenated functional groups while introducing nitrogen atoms, leads to slightly lower H_2O_2 selectivity. In a carbon matrix with enriched edges possessing oxygenated groups, P-doping significantly impacts ORR. In an alkaline medium, undoped GNRs with more defects and enriched oxygenated edges are more efficient in promoting ORR via the 2-electron ($2e^-$) pathway. Conversely, GNRs with higher nitrogen content and oxygen groups distributed across the basal plane prefer the 4-electron pathway. Maintaining high oxygen content and introducing phosphorus atoms into the GNR matrix are crucial for enhancing ORR performance and selectivity for H_2O_2 production.

Results and discussion

Material Characterization

Initially, Fourier transform infrared spectroscopy (FT-IR) was used to investigate the bulk properties and functional groups present in the GNR samples. Figure S1 shows the FT-IR spectra for the GNOs and GNRs developed in the study.

In general, FT-IR responses for the GNOs and GNRs showed peaks related to OH stretching vibration, OH stretching vibration from water, C–C stretching in rings, ring stretching mixed with C–H bending, and out-of-plane bending of the C–H bonds in rings[45,46] (Table S1).

The FT-IR spectrum of GNO1 was found to differ from that of GNR1; this can be explained by the presence of broad peak at 3,414 cm^{-1}, which is related to OH stretching vibration from water and a strong peak at 1,385 cm^{-1}, which is related to ring stretching mixed with C–H bending (Figure S1 and Table S1).

GNO2 and GNR2 were found to exhibit very similar FTIR spectra in comparison with GNR1 (Figure S1 and Table S1); this shows that both synthesis methods produced the same chemical groups found in GNO1, GNR1, GNO2, and GNR2.

When GNO1 and GNO2 were oxidized (GNO3 and GNO4, and reduced (GNR3 and GNR4)) for a second time, the unique difference observed between these two groups (before and after the second oxidation) was the nearly total absence of broad peak at 3,248 cm^{-1} and the exposure of a small broad peak at around 3,414 cm^{-1}, which are both related to OH stretching vibration from water (Figure S1 and Table S1); this again confirms that both methods produced the same chemical groups found in the samples.

To gain direct insights into the crystallinity and defects within graphene materials, including the identification of edges, we conducted Raman spectroscopy experiments. Figure 1 shows the Raman spectra obtained for the different GNRs investigated.

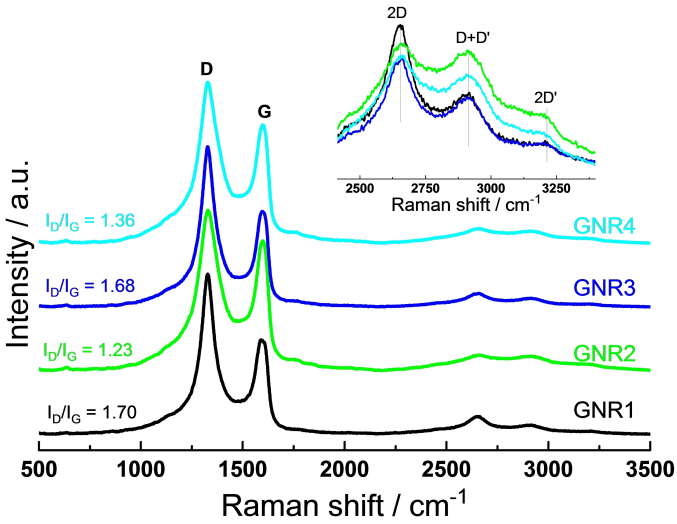

Figure 1. Raman spectra of the different GNRs investigated.

The Raman spectra reveal prominent first-order bands: the disorder band (D band) at approximately 1328 cm^{-1} and the graphite band (G band) at around 1598 cm^{-1}[6,47–50] (Table S2). Compared to the G band, the relatively higher intensity of the D band is indicative of the contribution of edge defects.[48] Furthermore, the I_D/I_G ratio, which signifies the relative intensity of the D and G bands, helps to confirm the varying degrees of defects observed across the samples.[33,49,51,52] Detailed I_D/I_G ratio values for the GNRs can be found in Table S2. These findings help solidify the observation that GNR1 and GNR3 exhibit a higher defect density than GNR2 and GNR4. Additionally, the Raman spectra reveal lower-intensity signals which correspond to double-resonant bands assigned to 2D,[53] D + D′,[53] and 2D′ bands at approximately 2657, 2919, and 3213 cm^{-1}, respectively[12,48,54,55] (Table S2). Typically, the 2D band is found to be a valuable metric as it helps one to discern the variations in sheet stacking and graphene layer count.[56,57] The inset of Figure 1b shows that GNR1 and GNR3 exhibit markedly more intense peaks, which signify a higher degree of stacking. This high peak intensity is indicative of the presence of a greater number of sheets or ribbons in these particular samples. The D + D′ and 2D′ bands observed in the Raman spectra are associated with disorder-induced and second-order Raman overtone of damaged graphene.[58] The shift of these bands toward higher wavelengths points to a higher level of disorder in the GNR1 and GNR3 samples compared to the GNR2 and GNR4 samples (as depicted in Table S2). Furthermore, the presence of some GNR multi-layers in the samples contributed to the emergence of a distinct peak at approximately 2919 cm^{-1}(D + D′ band) – which is a characteristic feature of graphene.[48] The observed shifts in the band positions (Table S2) reflect structural changes induced by the different methods of opening multi-walled carbon nanotubes (MWCNTs).[28] These disparities in the Raman results can be attributed to the oxidative power of Method 2, which leads to the extensive opening of MWCNTs to the extent of fusing their edges, resulting in wider graphene ribbon structures and a reduced number of edges compared to Method 1. Conversely,

Method 1 opens the MWCNTs to a degree that allows for the formation of GNRs with more clearly defined edges. Overall, Method 2 exhibits a more pronounced level of chemical oxidation, primarily attributed to the extended exposure of MWCNT to concentrated H_2SO_4 – lasting nearly twice as long (14 h), and the use of 1.7 times the mass of $KMnO_4$ (2 h) compared to Method 1, which involves an 8-hour treatment with concentrated H_2SO_4.

X-ray Photoelectron Spectroscopy (XPS) was used to analyze the chemical composition and elemental distribution within the GNRs. The XPS survey spectra (Figure S2) distinctly reveal the presence of specific peaks, including C 1s and O 1s, with binding energies at 285 eV and 534 eV, respectively, across all the samples investigated. Additionally, a minor O KLL peak at 975 eV is observed in all the samples. For a quantitative analysis of the XPS data, we calculated mass content percentages of the samples, as shown in Table S3; as can be noted, on average, GNR1 and GNR3 contain 85.3% carbon (C 1s) and 14.7% oxygen (O 1s), while GNR2 and GNR4 are composed of 82.6% carbon (C 1s) and 17.4% oxygen (O 1s). These results are in line with those obtained from the elemental analyses presented in Table S4, where GNR1 and GNR3 exhibit average mass content percentages of 77.5% carbon and 11.3% oxygen, whereas GNR2 and GNR4 exhibit mass content percentages of 63.2% carbon and 23.7% oxygen.

The elemental analysis (EA) results, as summarized in Table S4, provide valuable insights into the oxidation and subsequent reduction processes applied to the samples, and shed light on the changes that occurred in their elemental composition. Overall, compared to the MWCNTs, a noticeable increase is observed in the oxygen content of all the GNR samples; this increase in oxygen content points to the occurrence of a successful oxidation process which enriched the samples with oxygen functionalities. Following the oxidation, a reduction process was employed; this process led to a reduction of the oxygen content in the GNRs compared to their oxidized counterparts (GNOs). Regarding the content of N, it is evident that the reduction process involving the use of hydrazine led to an anticipated increase in nitrogen content in the GNRs compared to the oxidized GNOs. Specifically, GNR1 and GNR3 are found to exhibit lower residual nitrogen content compared to GNR2 and GNR4; this reflects variations in the reduction efficiency between the different samples investigated. All the samples recorded a minor increase in hydrogen content after the chemical reduction process (c.f. Table S4); this points to its minor role in the reduction of oxygen functionalities. In contrast, the presence of sulfur is found to be negligible in all samples; this points to its minimal impact on the elemental composition of the materials. In summary, the EA results highlight the effectiveness of the oxidation and reduction processes in modifying the elemental composition of the GNR samples, particularly in terms of oxygen and nitrogen content.

In line with previous findings reported in the literature, the results obtained from the thermogravimetric analysis (TGA) conducted in this study provide valuable insights into the thermal stability of the GNRs and how it is influenced by their oxidation and reduction processes.[59–61] Firstly, it is noteworthy that GNR3 exhibits a relatively higher degree of stability compared to GNR1, as evidenced by the region with higher temperature related to the effective mass loss curve (Figure S3a). This improved stability in GNR3 is attributed to the second oxidation process, which enhances its resistance to thermal degradation. Also, GNR2 displays a higher degree of stability compared to GNR1, with a burnout temperature reaching approximately 655 °C. This difference can be attributed to the wider graphene ribbon structures with a reduced number of edges in GNR2, which tends to render the sample less susceptible to thermal degradation. Following the second oxidation, GNR4 is found to exhibit reduced resistance to burning when compared to GNR2, as evidenced by the region with lower temperature related to the effective mass loss curve (Figure S3a). This observation further points to the influence of the oxidation process on the thermal properties of GNRs. Under N_2 atmosphere, GNR1 and GNR3 demonstrate greater stability compared to GNR2 and GNR4 (Figure S3b). This higher stability can be attributed to the presence of additional oxygen content in the latter two catalysts (Table S4), which renders them more susceptible to pyrolysis.

Figure 2 shows the high-resolution XPS spectra obtained for the GNR samples.

The C 1s HR-XPS spectra show a very accentuated peak and a shoulder (Figure 2) that are deconvoluted into four peaks – attributed to the chemical states C=C & C–C, C–OH & C–O–C, C=O & COOH, and π–π positioned on average at 284.8, 286.2, 288.3, and 290.5 eV, respectively (Table S5). Overall, our results are in agreement with the results reported in the literature.[15–17,23,61–63] In terms of % content, the lowest contribution came from π–π chemical states; however, after the second oxidation, we observed a decrease in % content coming from C=C & C–C between GNR1 and GNR3 (33.2 to 21.9) and a markedly significant decrease between GNR2 and GNR4 (50.9 to 28.1). In addition, a significant decrease in % content coming from C=C & C–C was also recorded between GNR2 and GNR1 (50.9 to 33.2) (Table S5). These observations help confirm that the structures of GNR2 and GNR4 have less defects/more C=C & C–C structures than the GNR1 and GNR3 structures; this is in agreement with the Raman results (Figure 1). It should be noted however that, after the second oxidation, both the GNR3 and GNR4 structures were found to exhibit more defects/less C=C & C–C structures compared to the GNR1 and GNR2 structures, respectively (Table S5).

The O 1s HR-XPS spectra show a broad peak (Figure 2) which is deconvoluted into three peaks–attributed to the chemical states of C=O, C–O, and H_2O, and positioned on average at 532.2, 534.2, and 536.5 eV,[15–17,23,61–63] respectively (Table S5). The main contribution in terms of % content comes from C=O and C–O chemical states with an average of 69.5% for GNR1 and GNR3 and 82.1% for GNR2 and GNR4. This observation points to the presence of more oxidized structures for GNR2 and GNR4 catalysts, where the major content comes mainly from C–O bond. The C–O bonds are typically associated with oxygenated functional groups, which are predominantly situated along the edges of carbon-based materials.

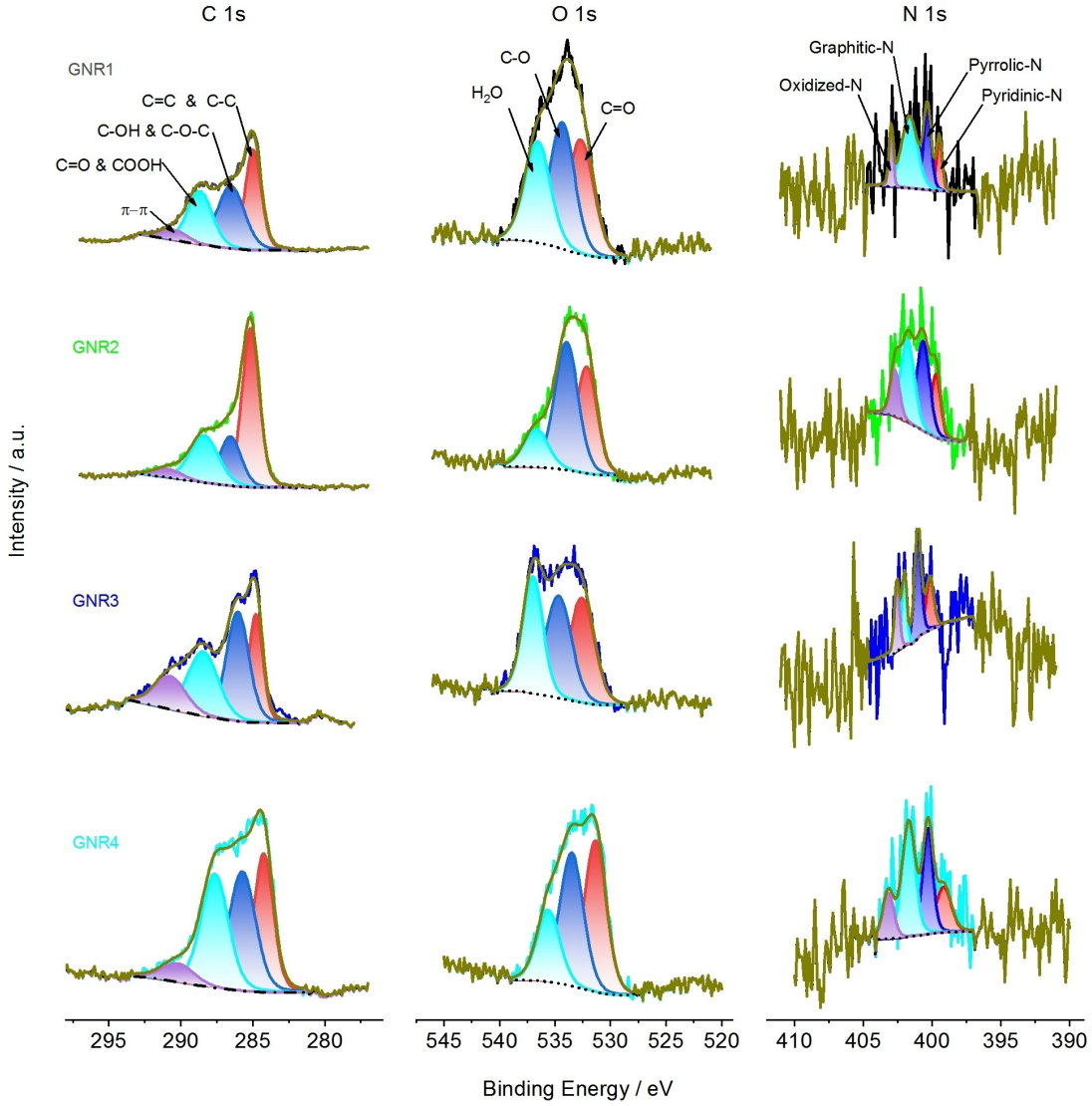

Figure 2. HR-XPS curves for the GNR samples investigated in this study.

Figure 2 also shows the HR-XPS spectra for the N 1s region. Although some GNR samples are found to exhibit low signal-to-noise ratio due to their low nitrogen content, one can clearly observe the presence of a broad peak. This peak is found to be deconvoluted into the pyridinic-N, pyrrolic-N, graphitic-N, and oxidized-N peaks,[14–16,23] as indicated in Table S5; here, the predominant contributors in terms of % content are the graphitic-N and pyrrolic-N functional groups, which constitute approximately 35.7% and 32.8% (on average), respectively. Coming closely behind these peaks are the pyridinic-N and oxidized-N groups, which constitute approximately 17.7% and 13.9% (on average), respectively.

Figure S4 shows the HR-XPS spectra for P 2p, S 2p, Cl 2p, Mn 2p, and Fe 2p, which are constituted mostly of noise; these spectral data help to confirm the following: i) the P and S elements exhibited low signal, not allowing us to quantify them; and ii) low amounts of contaminants (Cl, Mn, and Fe) remained in the samples at the end of the different GNR synthesis processes.

The TEM images in Figure 3 provide us with a clear visualization of the GNR structures resulting from the opening of MWCNTs. The GNR1 and GNR3 catalysts exhibit abundant edges within their structures which are indicative of well-defined graphene nanoribbons. In contrast, the GNR2 and GNR4 catalysts can be found to exhibit not only opened MWCNT structures but also large graphene sheets. The second method applied for the opening of the MWCNTs (Method 2) is found to be more effective in producing graphene ribbons with higher oxygen content within the basal carbon matrix; interestingly, this method also results in fewer edges, as indicated by the EA and Raman results, where higher oxygen content correlates with lower degree of defects, which is represented by a lower I_D/I_G ratio. Furthermore, our TEM findings also point to the presence of more extensive graphene sheets with fewer edges in GNR2 and

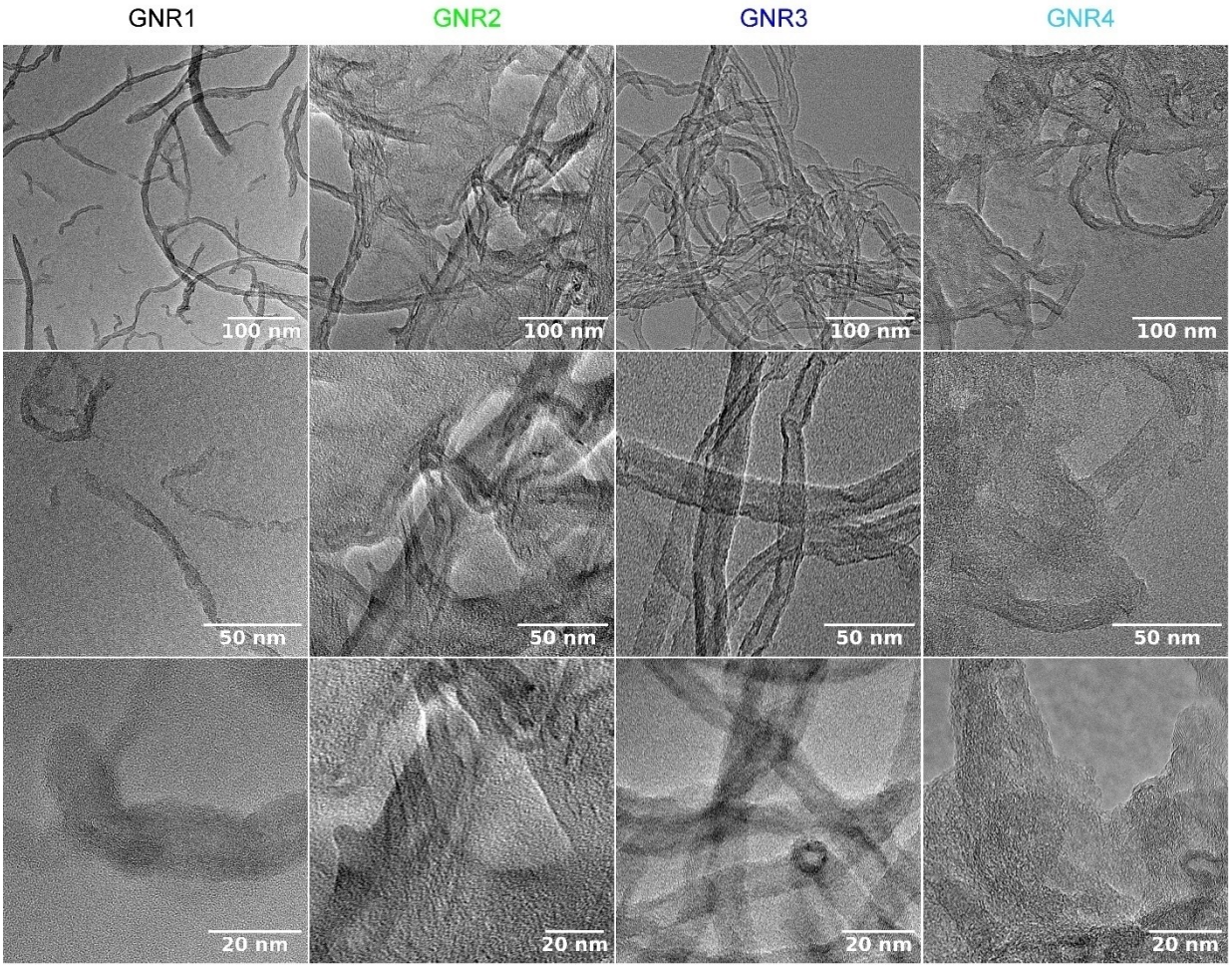

Figure 3. TEM images of the different GNRs investigated in this study.

GNR4 compared to the other samples. This structural distinction reflects the overall performance pattern observed in our study.

Electrochemical Study – CV Profile and ECSA

Figure S5 shows the cyclic voltammetric curves (CV) recorded for the undoped and doped GNR samples using N_2-saturated 0.5 M H_2SO_4 and 0.1 M KOH electrolyte solutions. For an in-depth analysis of the CV profiles and a comprehensive discussion of the capacitance and electrochemically active surface area (*ECSA)* values for the different undoped and doped GNRs, please refer to the Supplementary Information.

ORR Activity and Selectivity in Acidic Medium

To evaluate the ORR activity and selectivity of both the undoped and doped GNR samples, we conducted linear sweep voltammetry (LSV) experiments with a rotating ring-disk electrode (RRDE) setup. These experiments were performed in O_2–saturated 0.5 M H_2SO_4 and 0.1 M KOH electrolyte solutions, and the results obtained are presented in Figure 4a–f. Based on the LSV curves obtained using the disk and ring electrodes, we calculated the selectivity toward H_2O_2 production (X_{H2O2}) and the number of electrons transferred during the ORR process (n_{av}) at varying potentials. The average values obtained for X_{H2O2} and n_{av} are summarized in Table 1. Detailed curves can be found in Figures S10–11 in the SI.

Analysis in Acidic Medium

In acidic medium, the LSV curves obtained for the undoped GNRs (Figure 4a) showed that two of the samples, GNR3 and GNR4 catalysts, which underwent two oxidation processes for the opening of the MWCNTs, exhibited a slightly improved ORR activity; these two samples, namely, GNR3 and GNR4, exhibited an onset potential (E_{onset}) of 0.28 and 0.29 V, respectively, while GNR1 and GNR2 recorded E_{onset} values of 0.24 and 0.26 V, respectively. For the analysis of selectivity (c.f. Table 1 and Figures S10–11), it was evident that the GNR3 and GNR4 catalysts favoured the 2-electron ($2e^-$) pathway during ORR; on average, these catalysts exhibited 87% selectivity toward H_2O_2 production (X_{H2O2}) and had a corresponding number of electrons (n_{av}) of ca. 2.3, on average. In contrast, GNR1 and GNR2 exhibited an

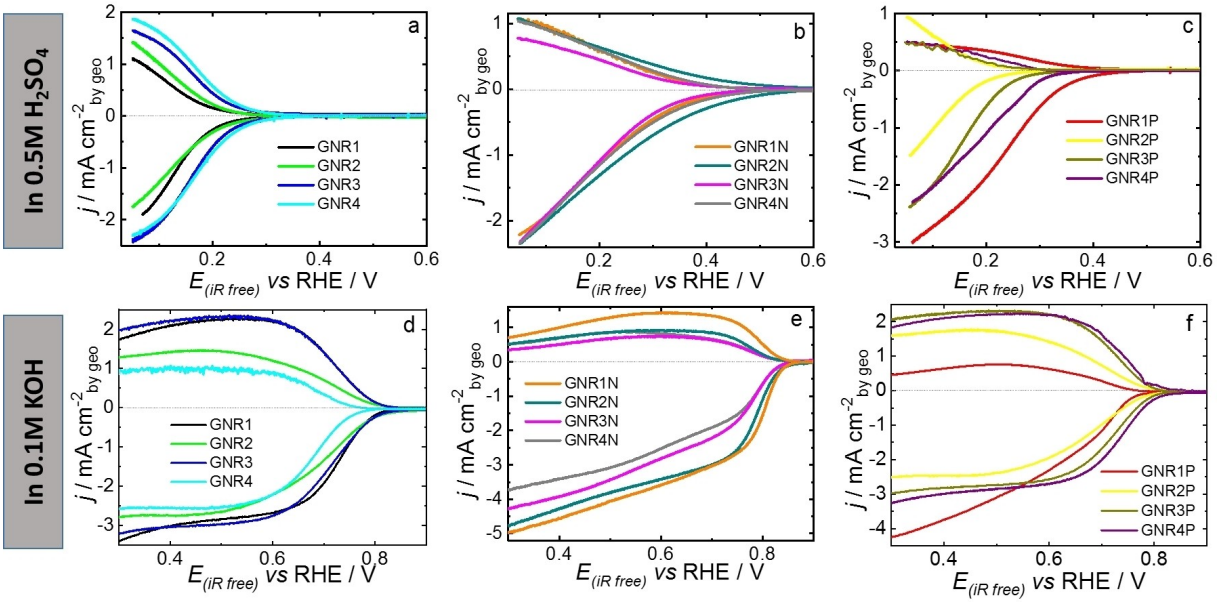

Figure 4. Results obtained from the linear sweep voltammetry (LSV) analysis conducted using a RRDE setup for GC electrodes modified with 150 μg cm^{-2} of undoped or doped GNR catalysts. The analyses were performed under the following conditions: potential scanning rate set at 10 mV s^{-1}; RRDE rotation speed at 1600 rpm; electrolyte solutions employed were: O_2–saturated 0.5 M H_2SO_4 and 0.1 M KOH. Scans were initiated at either 0.05 V or 0.3 V.

average X_{H2O2} of approximately 80% and n_{av} value of ca. 2.4. We hypothesize that the enhanced performance of the undoped GNR3 and GNR4 samples in H_2O_2 production in acidic media may be attributed to the higher oxygen content in GNR3 compared to GNR1 and the increased number of defects or edges in GNR4 in comparison with GNR2.

As shown in Figure 4b, after N-doping, a significant improvement was observed in the ORR catalytic performance of all the doped-GNR samples compared to their undoped counterparts. The most substantial improvement in ORR activity was observed in GNR2N; this sample exhibited an onset potential (E_{onset}) of 0.49 V, indicating a remarkable catalytic gain of 230 mV compared to the undoped GNR2, as highlighted in Table 1. Regarding selectivity toward H_2O_2 production, the X_{H2O2} values obtained for the N-doped GNR samples recorded an average X_{H2O2} value of 71%, with corresponding n_{av} of ca. 2.5. The slightly lower average X_{H2O2} values recorded for the doped samples compared to the undoped samples can be attributed to the concurrent reduction in oxygenated functional groups which occurred during the N-doping process, along with the introduction of nitrogen atoms. The increase in ORR activity coupled with a relatively high H_2O_2 production rate ($X_{H2O2} \approx 79\%$) observed for GNR2N can be attributed to the utilization of a GNR sample that inherently contains a higher amount of oxygenated groups – such as quinones, epoxides, and hydroxyl groups, within the basal carbon matrix, while having fewer edge sites. After N-doping, some of these oxygen groups in the basal carbon matrix are replaced by N atoms, resulting in an N-doped version of GNR with a higher amount of graphitic- and oxidized-N groups. These heteroatom groups are known to enhance ORR activity, and this helps explain the observed improvements in catalytic performance.[64–66] Yang et al.[67] found that iron atoms dispersed in hollow porous nitrogen-doped carbon capsules (H–Fe–Nx–C) were able to present a $E_{1/2}$ (vs. RHE) of 0.90 V, mainly producing water during ORR.

Regarding the P-doped GNR samples, significant variations were observed in the ORR activity. Specifically, the GNR1P sample (Figure 4c) exhibited the most significant improvement in ORR activity among the samples, recording E_{onset} value of 0.46 V. The GNR2P sample exhibited lower ORR activity, recording E_{onset} value of 0.26 V, which was even inferior to the performance of the undoped GNR2, as indicated in Table 1. In terms of selectivity toward H_2O_2 production, the P-doped GNR samples recorded an average X_{H2O2} value of 39% ($n_{av} \approx 3.2$). The discrete improvement observed in ORR activity, combined with relatively low selectivity toward H_2O_2 production, can be associated with the lower electronegativity of phosphorus atoms compared to carbon. Phosphorus is less effective than nitrogen in terms of modulating the charge densities of carbon, and this causes discrete changes in oxygen adsorption in the carbon structure, particularly in acidic medium. These findings are in line with the findings of our previous study, as reported in.[14] In the case of P-doping, the presence of a higher concentration of edges in a GNR matrix and an increased amount of oxygen groups on these edges likely facilitate the insertion of phosphorus atoms into the GNR structure, and this enhances the catalytic activity, particularly in acidic environments, through a 4-electron pathway. The method involving the opening of the MWCNTs (Method 1) which led to the formation of GNRs with more edges enriched with oxygen atoms (Method 1) likely facilitated the insertion of phosphorus atoms into the GNR matrix, contributing to the observed enhancement in catalytic performance of GNR1P.

On the other hand, Method 2, which promotes a broader distribution of oxygen atoms across the basal plane of the GNR and results in fewer exposed edges, hinders the incorporation of phosphorus atoms into the carbon matrix due to the difficulty in

Table 1. Comparative analysis of the ORR parameters of the undoped and doped GNR catalysts in different media. The table provides the following relevant data for the catalysts investigated: ORR onset potential values (E_{onset}, data obtained from Figure 4), selectivity toward H_2O_2 production (X_{H2O2}, data obtained from Figure S10), number of electrons transferred during ORR (n_{av}, data obtained from Figure S11), and Tafel plots (data Figure 4 obtained from Figure S12).

Catalyst	Electrolyte	E_{onset} $[V_{RHE}]$[a]	X_{H2O2} [%][b]	n_{av}[b]	Tafel slope [mV dec^{-1}]
GNR1	0.5 M H_2SO_4	0.24	76.2	2.5	90
GNR1	0.1 M KOH	0.82	87.4	2.3	61
GNR2	0.5 M H_2SO_4	0.26	83.3	2.3	109
GNR2	0.1 M KOH	0.85	63.1	2.7	99
GNR3	0.5 M H_2SO_4	0.28	84.1	2.3	90
GNR3	0.1 M KOH	0.83	89.7	2.2	78
GNR4	0.5 M H_2SO_4	0.29	89.5	2.2	89
GNR4	0.1 M KOH	0.77	60.3	2.8	66
GNR1N	0.5 M H_2SO_4	0.41	69.0	2.6	147
GNR1N	0.1 M KOH	0.85	51.1	3.0	37
GNR2N	0.5 M H_2SO_4	0.49	78.7	2.4	144
GNR2N	0.1 M KOH	0.85	35.1	3.3	52
GNR3N	0.5 M H_2SO_4	0.39	59.3	2.8	142
GNR3N	0.1 M KOH	0.86	30.2	3.4	65
GNR4N	0.5 M H_2SO_4	0.43	78.2	2.4	157
GNR4N	0.1 M KOH	0.84	40.4	3.2	60
GNR1P	0.5 M H_2SO_4	0.46	35.3	3.3	132
GNR1P	0.1 M KOH	0.78	40.3	3.2	60
GNR2P	0.5 M H_2SO_4	0.24	63.9	2.7	91
GNR2P	0.1 M KOH	0.80	86.6	2.3	78
GNR3P	0.5 M H_2SO_4	0.28	23.5	3.5	87
GNR3P	0.1 M KOH	0.81	92.5	2.2	57
GNR4P	0.5 M H_2SO_4	0.32	31.5	3.4	71
GNR4P	0.1 M KOH	0.83	92.3	2.2	66

[a] The E_{onset} values were determined based on the point at which the disk current density reached −0.1 mA cm^{-2}. [b] The X_{H2O2}(%) and n_{av} values were calculated (see equations S1–2) within the potential range starting from the lower potential (the potential at which the LSV curve begins) and extending to the onset (E_{onset}) potential.

inserting a larger heteroatom into the basal plane of the carbon; consequently, this method exerts limited influence on the oxygen reduction reaction (ORR) process in acidic environments. It is worth noting that the reduction in oxygen content, as observed through elemental analysis, is not as pronounced for GNR2P as it is for GNR1P (c.f. Table S4). These observations are in good agreement with the electrochemical results and Raman spectroscopy data (c.f. Tables S2 and S4). In light of these findings, it becomes evident that, for P-doping to have a significant impact on ORR, it would be advantageous to use a carbon matrix that possesses a greater amount of edges enriched with oxygenated groups.

Analysis in Alkaline Medium

In alkaline medium, the LSV curves obtained for the undoped GNRs (Figure 4d) showed that the GNR1 and GNR3 catalysts exhibited the highest ORR activity along with high selectivity toward H_2O_2 production, with an average E_{onset} of 0.83 V and X_{H2O2} of 89% ($n \approx 2.2$), as can be found in Table 1. In contrast, the GNR2 and GNR4 catalysts, which contained a higher oxygen content, ca. 24 wt.%, on average (c.f. Table S4), exhibited lower ORR activity; these catalysts recorded E_{onset} values of 0.85 and 0.77 V, respectively, along with an average X_{H2O2} of 62% ($n \approx 2.8$). In addition, the GNR2 and GNR4 catalysts demonstrated diffusion-limited current densities which were approximately 20% lower than those of the GNR1 and GNR3 samples, on average. These results suggest that, for the undoped GNRs, a graphene matrix with more defects and an increased presence of edges enriched with oxygen groups (as seen in GNR1 and GNR3) is more efficient in promoting ORR via the 2-electron ($2e^-$) pathway in alkaline medium compared to a matrix containing oxygen more widely distributed in the basal plane (as seen in GNR2 and GNR4).

In the case of N-doped GNR samples, we noted the occurrence of a more pronounced improvement in ORR catalytic performance for the GNR4N sample (Figure 4e) compared to their undoped counterparts (Figure 4d). However, among the N-doped samples, the highest ORR activity was observed for the GNR1N and GNR2N catalysts, where both exhibited E_{onset} of 0.85 V; these catalysts also presented selectivity toward H_2O_2 production of 51% ($n_{av} \approx 3.0$) and 35% ($n_{av} \approx 3.3$), respectively. The relatively higher selectivity observed for the GNR1N sample can be attributed to its lower N content (3 wt.%, c.f. Table S4) which is more strictly distributed on the edges – this likely includes a higher proportion of pyridinic-N and pyrrolic-N groups and most probably some edge graphitic-N (see Table S5 in Cardoso et al.,[14] since GNR1N is the similar GNRN catalyst in that reference). Furthermore, the GNR1N sample is also found to contain oxygenated groups (4 wt.%). In contrast, GNR2N exhibited 9 wt.% N content and a higher amount of oxygen content (11.5 wt.%); this observation can be related to the presence of a higher quantity of oxygen groups distributed widely across the basal plane of GNR2N, coupled with the presence of fewer edges, which favour the preferential ORR 4-electron pathway. These results suggest that a GNR matrix with more defects and an increased presence of edges enriched with oxygen groups is more efficient in promoting ORR via the 2e-pathway in alkaline medium, while a GNR matrix with higher nitrogen content and oxygen groups distributed across the basal plane favour the occurrence of ORR via the 4-electron pathway. Zhang et al.[68] produced defect-rich N-doped ultranarrow graphene nanoribbons (DN-UGNR) oxidizing chemically and unzipping of carbon nanotubes (CNT), followed by ammonia injection at high temperature, obtaining mostly OH^- (≅90%) from ORR in alkaline solution.

Regarding the P-doped GNR samples in alkaline medium, we noted significant variations in ORR catalytic activity compared to other doped and undoped GNR samples. Specifically, the GNR4P and GNR3P samples (Figure 4f) were found to be the most active

surfaces when it comes to the promotion of ORR; these samples exhibited E_{onset} values of 0.83 V and 0.81 V, respectively. It should be noted however that, in the case of GNR3P, its E_{onset} value was lower than that of its undoped version (GNR3, $E_{onset} = 0.83$ V); this shows that ORR activation was not quite successful after P-doping in this GNR matrix. When it comes to selectivity (c.f. Table 1), both the GNR4P and GNR3P samples, which recorded X_{H2O2} of 92% ($n_{av} \approx 2.2$) and 93% ($n_{av} \approx 2.2$), respectively, favoured the occurrence of ORR via the 2e-pathway. In contrast, GNR1P and GNR2P exhibited the lowest ORR activity among the P-doped samples, recording an average E_{onset} value of 0.79 V and X_{H2O2} values of 40% ($n_{av} \approx 3.2$) and 87% ($n_{av} \approx 2.3$). These findings suggest that, when it comes to P-doping for the enhancement of ORR activity in alkaline media (compared to undoped GNRs), the successful scenario involves the application of GNR matrices with an abundant quantity of oxygen atoms that are widely distributed on the basal plane, as well as a certain concentration of edges containing oxygen groups which will help facilitate the insertion of phosphorus atoms into the GNR structure. Through a comparative analysis of the oxygen content across the samples (c.f. Table S4), we noted that maintaining a high oxygen content, alongside the insertion of phosphorus atoms into the GNR matrix, is crucial for enhancing ORR performance and selectivity toward H_2O_2 production.

It is worth pointing out that the Method 1 used to open the MWCNTs resulted in the formation of GNRs with an abundant quantity of oxygen-enriched edges. Some of these oxygen atoms remain in the matrix, enhancing ORR activity via the 2e-pathway, while others are removed or replaced after heteroatom-doping with N or P. Based on our results, we found that the use of GNRs with oxygen content concentrated at the edges facilitate the incorporation of phosphorus atoms into the GNR matrix, and this contributes to the enhancement in catalytic performance observed for the GNR1P and GNR4P samples. Notably, in the case of GNR4, the combination of both methods (Method 2 and Method 1) gave rise to a GNR matrix with two distinct characteristics: a considerable number of edges (c.f. Figure 4 and Table S2) and a higher oxygen content distributed throughout the sample, both on the basal and edge regions of the GNR. The wide distribution of oxygen across both the basal plane and edges of GNR4 proved beneficial, as it helped ensure the presence of a high concentration of oxygen groups throughout the sample while still enabling the insertion of phosphorus at the edges. This combined technique contributed to improvements in ORR activity and a high yield of H_2O_2. On the other hand, Method 2, which causes a broader distribution of oxygen atoms across the basal plane of the GNR and fewer edges, hinders the insertion of phosphorus atoms into the carbon matrix; however, this method favours N insertion into the carbon matrix, which results in improved ORR performance in both acidic and alkaline media, though it promotes lower selectivity toward H_2O_2 production (c.f. onset values in Table 1).

Figure 5 illustrates the effects of N- and P-doping on GNR4 in terms of ORR activity and selectivity. The relatively low ORR activity and intermediate degree of selectivity observed in the undoped GNR4 sample can be attributed to its high oxidation level (22 wt.% oxygen content, Table S4) and the relatively considerable amount of nitrogen (3.4 wt.%) which remains from the reduction of GNO4; it should be noted however that this carbon matrix has a significant number of edges and oxygen functional groups dispersed throughout both the basal and edge regions. This configuration helps to ensure the presence of a high concentration of oxygen groups throughout the sample, while still allowing for the insertion of nitrogen into the carbon structure and phosphorus mainly at the edges. Both factors contribute to improvements in ORR activity. As mentioned earlier, high yields of H_2O_2 are achieved by the insertion of the doping element in the sample while the presence of oxygen functional groups throughout the sample is preserved. The differences in ORR activity observed between the N and P-doped samples can be attributed to variations in electronegativity and the ability to modulate the charge densities of carbon.

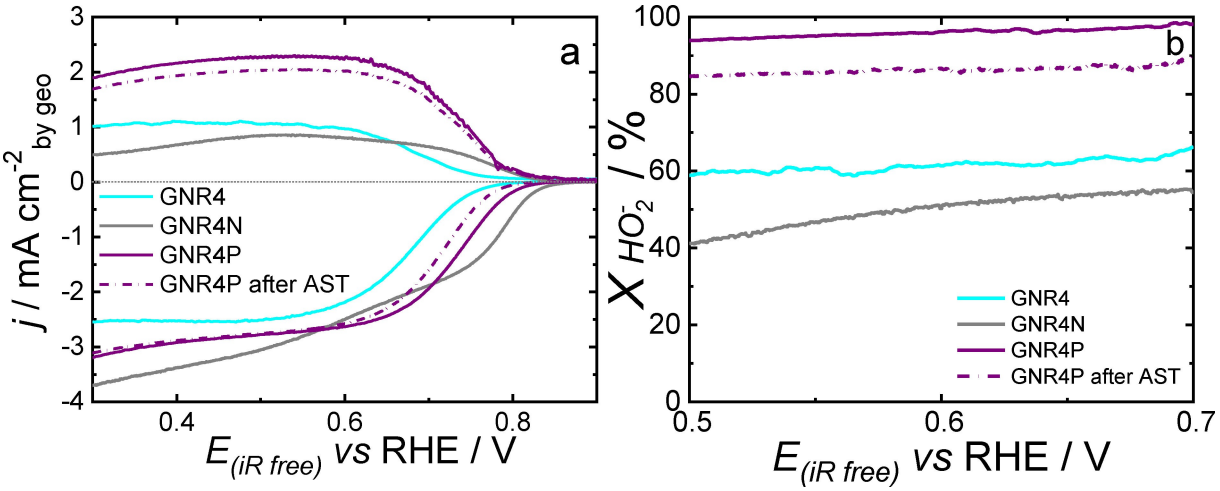

Figure 5. Results obtained from the linear sweep voltammetry (LSV) analysis conducted using a RRDE setup for GC electrodes modified with 150 μg cm^{-2} before AST of GNR4, GNR4 N, or GNR4P (before and after AST) catalysts. The analyses were performed under the following conditions: potential scan rate of 10 mV s^{-1}; RRDE rotation speed kept at 1600 rpm; electrolyte solution employed: O_2–saturated 0.1 M KOH. Scans were initiated at 0.3 V. The accelerated stress test (AST) comprised 10 000 CV cycles, ranging from 0.6 to 1.0 V at 50 mV s^{-1} in O_2–saturated 0.1 M KOH.

Phosphorus is less effective than nitrogen in terms of modulating the charge densities of carbon, and this allows for more favourable tuning of oxygen adsorption in the carbon structure, which helps preserve the integrity of the O=O bond. In terms of the mechanism, we can speculate that in our P-doped GNR4, molecular oxygen is adsorbed, in a Pauling-type form, in the carbon atoms near the oxygen and phosphorus atoms. This configuration facilitates the release of HOOH or OOH^- after the 2e-transfer in the ORR process.[69,70]

To evaluate the long-term stability of the GNR4P catalyst's ORR performance, we used an accelerated stress test (AST) that involved 10,000 potential cycles between 0.6 and 1.0 V. This procedure simulates the start-stop conditions associated with electrochemical H_2O_2 production devices. The stability test findings support the GNR4P catalyst's outstanding stability under such conditions. Figure 5a shows the minor variations in ring/disk current densities before and after AST. This adjustment results in a ~6% decrease in H_2O_2 production post-test, with average selectivity shifting from 92% to 86%, as shown in Figure 5b.

In general, the results obtained from the application of the samples in acidic media indicate that, despite being doped with N and P, the materials in this study exhibited considerably lower catalytic activity compared to state-of-the-art catalysts for both water generation and H_2O_2 generation in acidic conditions, such as Pt- and Pd-based catalysts.[71,72] However, the results obtained for GNR4P in alkaline medium were found to be comparable to or even better than those of established carbon-based catalysts for H_2O_2 production, as demonstrated in Table S8.

To gain a deeper understanding of the kinetics of these carbonaceous materials, Figure S12 displays the Tafel curves for the different doped and undoped GNRs investigated in this study, while Table 1 presents the corresponding Tafel slope values. Specifically, the Tafel slope values obtained for the synthesized materials range from 37 to 157 $mV\,dec^{-1}$, while the values for state-of-the-art catalysts are typically around 60 $mV\,dec^{-1}$; this variation is likely attributed to the presence of more intermediate steps in the reaction process, which overall delays the ORR process on the surfaces of the synthesized materials.

High Tafel slopes are found to be associated with high H_2O_2 selectivity for the catalysts investigated in this study, as observed in the cases of GNR2, GNR2N, and GNR4N samples. In general, the main reason for variations in catalyst activity between acidic and alkaline conditions lies in the differing availability of protons or hydroxide ions and intermediates in these distinct environments. The sluggish ORR activity observed on these surfaces in acidic media can be linked to the hindered interaction between molecular oxygen and the N and P-functional groups within the carbon matrix due to protonation.[20] The protonation of N and P groups on the catalyst surface may impede charge delocalization, thereby compromising electrocatalytic activity in acidic conditions and promoting the formation of H_2O_2 (due to the action of oxygenated functional groups).[14] In alkaline conditions, on the other hand, deprotonated functional groups have a negative charge, which facilitates the removal of OH^- ions and promotes the adsorption of O_2 on the surface of the carbon matrix, followed by its subsequent reduction.

Conclusions

The present study offers valuable insights into the production and application of graphene nanoribbons (GNRs), derived from multi-walled carbon nanotubes (MWCNTs), as electrocatalysts for ORR in both acidic and alkaline environments. The findings of this study have highlighted the pivotal role played by the chosen MWCNT opening method in shaping the structural characteristics of GNRs, including edge density and oxygen atom distribution, which, in turn, exert a significant influence over the efficiency of N and P doping. Our findings point to the need for optimizing GNR structures and heteroatom doping strategies in order to modulate ORR electrocatalytic performance for specific environmental conditions. When MWCNTs are opened using a method that results in a broader distribution of oxygen atoms across the basal plane of the GNR and fewer exposed edges, N-insertion through the carbon matrix becomes more favourable for catalytic activity; this configuration enhances ORR performance in both acidic and alkaline media but is associated with reduced selectivity toward H_2O_2 production. On the other hand, the application of a different opening method that generates GNRs with a substantial number of edges and an extensive amount of oxygen functional groups spread across both the basal plane and edges has proven to be more advantageous; this second approach ensures a high concentration of oxygen groups throughout the sample while still facilitating phosphorus insertion at the edges. Based on the findings of this study, the application of the second approach is found to lead to improved ORR activity and a higher production of H_2O_2. Overall, the present study underscores the importance of the MWCNT opening method in modulating the structural characteristics of GNRs and, subsequently, their electrocatalytic behaviour. The findings of this study provide meaningful insights into ways to optimize carbon materials for application in electrocatalytic processes, particularly in ORR, and a suitable pathway toward the construction and design of highly efficient, tailored catalysts.

Experimental part

Reagents and Instruments

The compounds employed in the experiments included the following: potassium persulfate ($K_2S_2O_8$, 99% purity), hydrogen peroxide (H_2O_2, 30%), phosphorus pentoxide (P_2O_5, 99%), sodium nitrate ($NaNO_3$, 99%), and ammonia hydroxide (NH_4OH) solution (28 wt% in H_2O) (all of which were acquired from Vetec). Sulfuric acid (H_2SO_4, 98%), potassium hydroxide (KOH), and hydrochloric acid (HCl) were purchased from Merck. Potassium permanganate ($KMnO_4$, 98%) was obtained from Nuclear. Hydrazine sulfate ($NH_2NH_2.H_2SO_4$, 99%) and multi-walled carbon nanotubes (MWCNTs), with a dimension of 10 ± 1 nm (external diameter)×4.5 ± 0.5 nm (internal diameter) and 3–6 μm long with six to

eight tube walls, were acquired from Aldrich. The water employed in the experiments was obtained from reverse osmose equipment with resistivity higher than 18 MΩ cm and a temperature of 25 °C.

Electrode Preparation

The glass carbon (GC) disk was polished with alumina paste (1 mm) and sonicated in ultrapure water (Gehaka, resistivity > 18 MΩ cm) and acetone for 5 min in each solvent; this procedure was executed prior to conducting the electrochemical measurements. In an atmosphere of supra pure N_2, 10 cyclic voltammetry scans were carried out in the potential range of 0.05–1.2 V at 50 mVs^{-1} using 0.1 M $HClO_4$ solution; this was used to verify the cleanness of the GC disk surface. Also, 200 cyclic voltammetry scans were performed in the same potential range (of 0.05–1.2 V) at 900 mVs^{-1}; this was used to verify the cleanness of the Pt ring. The disk and ring were washed in ultrapure water and dried with N_2 flow. A uniformly thin catalyst film of 150 $\mu g\,cm^{-2}$ was produced on the electrode surface by dripping 30 μL of 1.0 $mg\,mL^{-1}$ aqueous (only water was used as a solvent) dispersion with the different catalysts investigated and allowing it to dry at room temperature. Each modified electrode was immersed in ultrapure water before being placed in the electrochemical cell containing an aqueous solution of 0.1 M KOH or 0.5 M H_2SO_4 in high-purity N_2 or O_2 (both purchased from White Martins), which was used to saturate the solutions.

Apparatuses, Measurements, and Material Characterization

The electrochemical measurements were performed in a three-electrode glass cell with a working electrode which consisted of a Teflon-embedded GC disk/Pt ring rotating assembly (0.196 and 0.11 cm^2 in geometric area, respectively) (Pine Research Instrumentation), with a collection efficiency of N = 0.26 – based on the manufacturer's information. A graphite rod and a reversible hydrogen electrode (RHE) were employed as counter electrode and reference electrode, respectively.

To perform cyclic voltammetry (CV) and hydrodynamic linear potential (HLS) scans, an AFP2 WaveDriver 20 – galvanostat bipotentiostat (Pine Research Instrumentation) was used, connected to an AFMSRCE speed modulated rotator. A PGSTAT128N potentiostat-galvanostat (Autolab) equipped with the FRA2.X module was used during the electrochemical impedance spectroscopy (EIS) experiments. EIS measurements were performed using 0.5 M H_2SO_4 and 0.1 M KOH in the frequency range of 10 mHz to 100 kHz and disturbance potential of 10 mV (rms). Ohmic drop resistance, adjusted from a high-frequency EIS intercept, was used to correct each HLS curve.

For the acquisition of Fourier transform infrared spectra (FT-IR), a Bomen FT-IR MB-100 spectrophotometer was used in the spectral window of 400 to 4000 cm^{-1}. Samples (catalysts) were prepared using dry material (~30 μg) and KBr (35 mg); the mixture was ground in order to obtain a fine, homogeneous powder. Thereafter, the powder was pressed, giving rise to a translucent tablet.

A LabRam HR Evolution micro-Raman spectrometer (Horiba Jobin-Yvon) was used to obtain the Raman spectral data at room temperature (25 °C); this was done using a solid-state laser operating at 633 nm, a standard grid (600gr/mm) and an EMCCD detector (Synapse EM). The samples were excited with a low-intensity laser (2 mW) to avoid overheating and the occurrence of photochemical phenomena. A 100 objective (Olympus, MPlan N) was used to focus the laser on the sample. The spectra were collected in an acquisition time of 12 seconds.

The PHI Quantera II (for surface analysis) was used for the conduct of XPS analyses. The Al Kα line (1486.6 eV) was used as the ionization source, which operated at 15 kV and 25 W. After performing background subtraction, the spectra were deconvoluted using a combination of Lorentzian (30 %) and Gaussian Voigt (70 %).

Elemental analysis (EA) was performed using Scientific Flash 2000 CNHS/O Elemental Analyzer Thermo Equipment under cycle operating conditions (run time) of 720 s and oven temperature of 950 °C for CHNS determinations and under the cycle (run time) of 400 s and oven temperature of 1060 °C for O determination.

The thermogravimetric characterization analyses were carried out in a Shimadzu TGA-50 thermogravimetric analyzer with a flow of FID Synthetic Air or N_2 5.0 gas (50 $mL\,min^{-1}$) at temperatures ranging from ambient to 900 °C, with a heating rate of 10 °C min^{-1}, using ceramic alumina crucibles.

The nanostructures of the catalysts were characterized by transmission electron microscopy (TEM) using JEM 2100F (JEOL) or Philips CM200, both operating at 200 kV.

Synthesis of Graphene Nanoribbon Oxide (GNO)

The GNOs were synthesized using two different methods (Scheme 1). Under Method 1, GNO1 was produced by a method adapted from Hummers and Offeman,[73] as reported by Lima and Maia[8] (Scheme 1, Method 1). The method involved the following: 0.70 g of MWCNT (used as received) was dispersed in 20 mL of concentrated H_2SO_4; after that, 0.37 g of $K_2S_2O_8$ and 0.37 g of P_2O_5 were added into the mixture, and the solution was heated at 80 °C for 6 h under stirring. The solution was then cooled to room temperature and 0 °C water was added therein. The product was then filtered under vacuum using a 0.22-μm Nylon membrane and was simultaneously washed with water in order to obtain a neutral pH. The resulting pre-oxidized graphene nanoribbon was dried at room temperature. The pre-oxidized graphene nanoribbon was re-oxidized using 40 mL of H_2SO_4, 0.70 g of $NaNO_3$ and 2.10 g of $KMnO_4$, with the solution kept at 0 °C. The mixture was kept at 35 °C for 2 h under stirring, and then 320 mL of ultrapure water at 5 °C and 40 mL of 30 % H_2O_2 were added into the mixture, which was then stirred for another 20 min. The solution was cooled to room temperature and transferred to a 3500 mL container containing ultrapure water at 0 °C. After 24 hours, the precipitate was centrifuged and washed twice with H_2O; this was followed by two cycles of washing with 90 : 10 H_2O/HCl v/v solution and another two cycles of washing

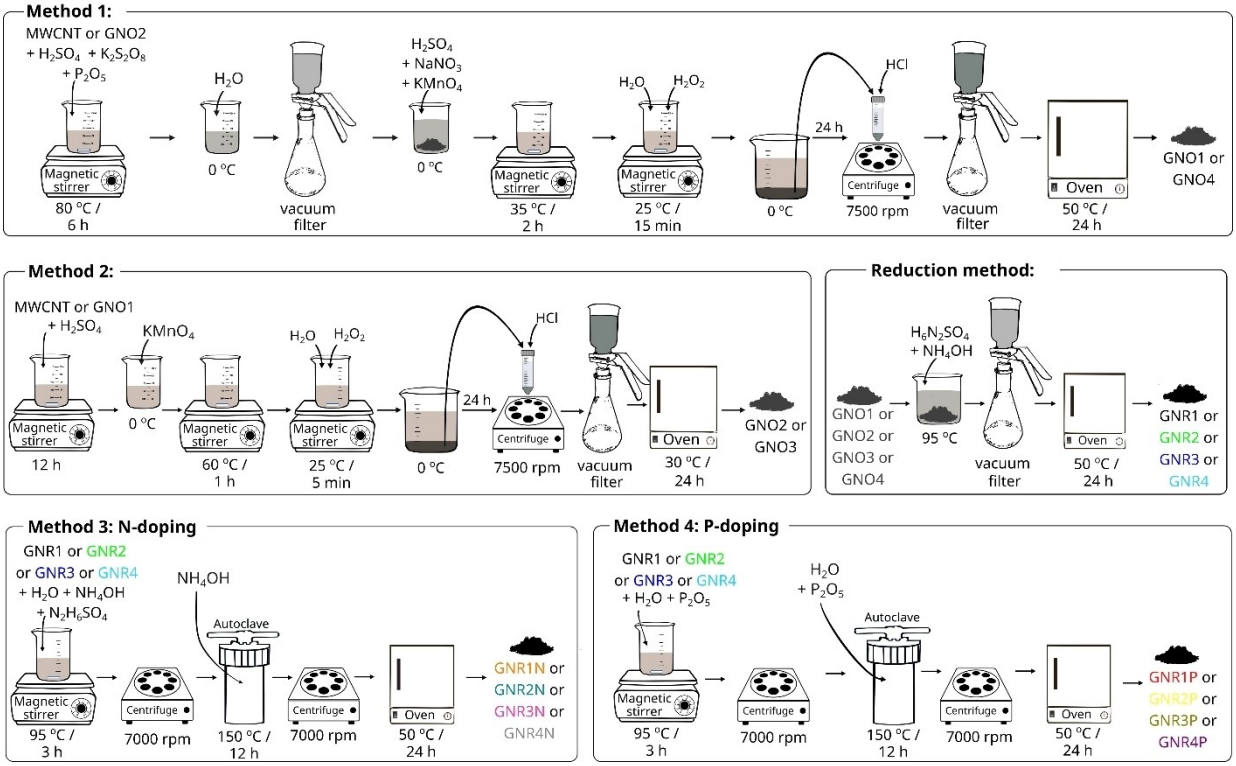

Scheme 1. Schemes illustrating the different synthesis methods adopted in this study. Method 1: production of GNO1 or GNO4. Method 2: production of GNO2 or GNO3. Reduction method: reduction of different GNOs (GNO1, GNO2, GNO3, or GNO4) to GNRs (GNR1, GNR2, GNR3, or GNR4). Method 3: N-doping of different GNRs (GNR1, GNR2, GNR3, or GNR4), giving rise to GNR1N, GNR2N, GNR3N, or GNR4N. Method 4: P-doping of different GNRs (GNR1, GNR2, GNR3, or GNR4), giving rise to GNR1P, GNR2P, GNR3P, or GNR4P.

using ultrapure H_2O. The material was subsequently subjected to filtration and washing with ultrapure water using a Nylon membrane until neutral pH was reached. Finally, the GNO1 was dried on a stove at 50 °C for 24 hours (Scheme 1, Method 1).

Under Method 2, GNO2 was produced based on the technique proposed by Tour *et al.*[6] (Scheme 1, Method 2). This method involved the following: a suspension was produced using 0.7 g of MWCNT in 30 mL concentrated sulfuric acid (H_2SO_4) under stirring for 12 hours. After that, an amount of 3.5 g of $KMnO_4$ was added into the mixture, which was then kept under stirring for 1 hour at room temperature and was subsequently heated at 60 °C for 1 hour. After this period, the mixture was then poured into 300 mL of a solution of 87% H_2O and 13% H_2O_2 at a temperature of 5 °C under constant stirring and then diluted with the addition of 3500 mL of cold ultrapure water and left idle for 24 hours. The mixture was centrifuged at 7500 rpm and washed with ultrapure water. The precipitate was then washed with 300 mL of aqueous HCl solution (90:10 H_2O/HCl, v/v) to remove metal ions, and this was followed by the application of three cycles of washing with a huge amount of ultrapure water in order to remove any acid and centrifuging the mixture at 7500 rpm. The product was filtered using 0.22 μm nylon film and was washed with ultrapure water to remove any residual acid until a neutral pH was obtained. The GNO2 was dried on a stove at 50 °C for 24 hours (Scheme 1, Method 2).

In addition, a portion of 0.5 g of GNO1 was treated using Method 2 described above (Scheme 1, Method 2), taking into account the stoichiometry of the mass variation of the starting material; this gave rise to GNO3. Likewise, 0.5 g of GNO2 was treated using Method 1, taking into account the stoichiometry of the mass variation of the starting material (Scheme 1, Method 1), and this gave rise to GNO4.

Synthesis of Reduced Graphene Nanoribbon (GNR)[8]

The method adopted for the reduction of the GNOs (GNO1, GNO2, GNO3, and GNO4) in order to obtain the GNRs (GNR1, GNR2, GNR3, and GNR4) involved collecting 250 mg of each of the GNOs separately and mixing each one of them with 5.0 mL of aqueous solution of hydrazine sulfate (21 mg) and 35 μL of ammonium hydroxide solution (28% by mass % in water) in a 20 mL glass vial. After being shaken vigorously for 30 minutes, the flasks were placed in a water bath (~95 °C) for 2 h and 30 min. The GNRs were obtained after vacuum filtration using a 0.22 μm Nylon film; they were then washed with 0.5% v/v ammonium hydroxide solution (100 mL). Excess ammonium hydroxide was removed by washing the mixture with ultrapure water until a neutral pH was obtained. The GNRs obtained were subsequently dried under vacuum at room temperature (Scheme 1, reduction method).

Synthesis of GNRs doped with Nitrogen (N) (GNR N)[14,23]

A hydrothermal route was employed for the N-doping (Scheme 1, Method 3) of the GNRs. In the N-doping synthesis, an amount of 20 mg of the corresponding GNR (GNR1, GNR2, GNR3 or GNR4) was used; the material was mixed with 30 mL of ultrapure water, 1 mL of ammonium hydroxide (28% by weight in water), and 1.06 g of hydrazine sulfate, and the mixture was subjected to an ultrasonic bath for 30 minutes. After that, the solution was heated at 95 °C for 3 h in a magnetic stirrer, and this was followed by the application of three cycles of washing with centrifugation (7000 rpm) using ultrapure water. The product obtained was mixed with 30 mL of ammonium hydroxide in a Teflon-coated autoclave and subjected to heating at 150 °C for 12 h; subsequently, the product was washed by centrifugation (7000 rpm) several times with ultrapure water and then dried in an oven at 50 °C. The resulting electrocatalysts were named GNR1N, GNR2N, GNR3N and GNR4N.

Synthesis of GNRs doped with Phosphorus (GNR P)[14]

In the P-doping synthesis (Scheme 1, Method 4), 20 mg of the corresponding GNR (GNR1, GNR2 GNR3 or GNR4) was used. This substance was mixed with 30 mL of ultrapure water and 200 mg of P_2O_5; the solution was subjected to an ultrasonic bath for 30 minutes and then heated at 95 °C for 3 h under constant stirring. The product obtained was then washed three times by centrifugation (7000 rpm) using ultrapure water. After that, the product was mixed with 30 mL of ultrapure water and 200 mg of P_2O_5 in a Teflon-coated autoclave and subjected to heating at 150 °C for 12 h; subsequently, the product was washed by centrifugation (7000 rpm) several times with ultrapure water and then dried in an oven at 50 C. The resulting electrocatalysts were named GNR1P, GNR2P, GNR3P and GNR4P.

Associated Content

Supporting Information. The supporting information contains experimental details, figures, equations, and tables related to supplementary results. The authors have cited additional references within the Supporting Information (Ref. [74–81]).

Acknowledgements

The authors would like to thank the following Brazilian research funding agencies for the financial assistance provided in support of this study: Brazilian National Council for Scientific and Technological Development – CNPq (grants #465571/2014-0, #302874/2017-8, #427452/2018-0, #303351/2018-7, #405742/2018-5, #380886/2020-0, #303943/2021-1, #302561/2022-6, #151161/2023-2), Fundect-MS (grants #71/020.168/2021, #71/027.195/2022 and #71/039.199/2022), CAPES-PRINT (grant #88881.311799/2018-01), and UFMS. São Paulo Research Foundation (FAPESP – grants #2014/50945-4, #2017/10118-0, #2019/04421-7, #2023/01425-7, and 2023/10772-2). E.S.F. Cardoso would like to extend his gratitude to PNPD-CAPES and Coordenação de Aperfeiçoamento de Pessoal de Nível Superior (CAPES – Finance Code 001) for the financial assistance provided during this research. M. Ledendecker would also like to acknowledge the Federal Ministry of Education and Research (BMBF) in the framework of NanoMatFutur (SynKat, FK: 03XP0265) for financial support. The authors would also like to thank the Laboratory of Structural Characterization (LCE/DEMa/UFSCar) for providing general facilities for the experiments.

Conflict of Interests

The authors declare to have no competing financial interests.

Data Availability Statement

The data that support the findings of this study are available from the corresponding author upon reasonable request.

Keywords: carbon nanotube · graphene nanoribbon · heteroatom-doping · hydrogen peroxide opening method · oxygen-reduction reaction

[1] Y. Gu, Z. Qiu, K. Müllen, *J. Am. Chem. Soc.* **2022**, *144*, 11499–11524.
[2] Z. Chen, A. Narita, K. Müllen, *Adv. Mater.* **2020**, *32*, 2001893.
[3] C. Huang, C. Li, G. Shi, *Energy Environ. Sci.* **2012**, *5*, 8848.
[4] M. Xu, T. Liang, M. Shi, H. Chen, *Chem. Rev.* **2013**, *113*, 3766–3798.
[5] J. Zhang, Z. Xia, L. Dai, *Sci. Adv.* **2015**, *1*, 1–19.
[6] D. V Kosynkin, A. L. Higginbotham, A. Sinitskii, J. R. Lomeda, A. Dimiev, B. K. Price, J. M. Tour, *Nature* **2009**, *458*, 872–6.
[7] N. Mohanty, D. Moore, Z. Xu, T. S. Sreeprasad, A. Nagaraja, A. A. Rodriguez, V. Berry, *Nat. Commun.* **2012**, *3*, 844.
[8] F. De Lima, G. Maia, *Nanoscale* **2015**, *7*, 6193–6207.
[9] J. Xu, X. Cui, N. Liu, Y. Chen, H. Wang, *SmartMat* **2021**, *2*, 202–212.
[10] R. Lv, M. Terrones, *Mater. Lett.* **2012**, *78*, 209–218.
[11] R. Cruz-Silva, A. Morelos-Gómez, S. Vega-Díaz, F. Tristán-López, A. L. Elias, N. Perea-López, H. Muramatsu, T. Hayashi, K. Fujisawa, Y. A. Kim, M. Endo, M. Terrones, *ACS Nano* **2013**, *7*, 2192–2204.
[12] A. Narita, X. Feng, Y. Hernandez, S. A. Jensen, M. Bonn, H. Yang, I. A. Verzhbitskiy, C. Casiraghi, M. R. Hansen, A. H. R. Koch, G. Fytas, O. Ivasenko, B. Li, K. S. Mali, T. Balandina, S. Mahesh, S. De Feyter, K. Müllen, *Nat. Chem.* **2014**, *6*, 126–132.
[13] L. Jiao, L. Zhang, X. Wang, G. Diankov, H. Dai, *Nature* **2009**, *458*, 877–80.
[14] E. S. F. Cardoso, G. V. Fortunato, C. D. Rodrigues, M. R. V. Lanza, G. Maia, *Nanomaterials* **2023**, *13*, 2831.
[15] E. S. F. Cardoso, G. V. Fortunato, G. Maia, *ChemElectroChem* **2018**, *5*, 1691–1701.
[16] E. S. F. Cardoso, G. V. Fortunato, G. Maia, *J. Phys. Chem. C* **2019**, *123*, 16308–16316.
[17] L. S. Bezerra, G. Maia, *J. Mater. Chem. A* **2020**, *8*, 17691–17705.
[18] Y. Li, W. Zhou, H. Wang, L. Xie, Y. Liang, F. Wei, J.-C. Idrobo, S. J. Pennycook, H. Dai, *Nat. Nanotechnol.* **2012**, *7*, 394–400.
[19] J. S. Lim, Y. J. Sa, S. H. Joo, *Cell Reports Phys. Sci.* **2022**, *3*, 100987.
[20] L. Yang, J. Shui, L. Du, Y. Shao, J. Liu, L. Dai, Z. Hu, *Adv. Mater.* **2019**, *31*, 1804799.
[21] H. S. Wroblowa, Yen-Chi-Pan, G. Razumney, *J. Electroanal. Chem. Interfacial Electrochem.* **1976**, *69*, 195–201.
[22] I. Katsounaros, W. B. Schneider, J. C. Meier, U. Benedikt, P. U. Biedermann, A. A. Auer, K. J. J. Mayrhofer, *Phys. Chem. Chem. Phys.* **2012**, *14*, 7384.
[23] E. S. F. Cardoso, G. V. Fortunato, I. Palm, E. Kibena-Põldsepp, A. S. Greco, J. L. R. Júnior, A. Kikas, M. Merisalu, V. Kisand, V. Sammelselg, K. Tammeveski, G. Maia, *Electrochim. Acta* **2020**, *344*, 136052.

[24] G. V. Fortunato, M. S. Kronka, E. S. F. Cardoso, A. J. Dos Santos, A. C. Roveda, F. H. B. Lima, M. Ledendecker, G. Maia, M. R. V. Lanza, *J. Catal.* **2022**, *413*, 1034–1047.
[25] J. Duan, S. Chen, M. Jaroniec, S. Z. Qiao, *ACS Catal.* **2015**, *5*, 5207–5234.
[26] D. W. Boukhvalov, M. I. Katsnelson, *Nano Lett.* **2008**, *8*, 4373–4379.
[27] S. K. Tiwari, S. K. Pandey, R. Pandey, N. Wang, M. Bystrzejewski, Y. K. Mishra, Y. Zhu, *Small* **2023**, *1*, 2303340.
[28] J. Wang, Z. Wu, L. Han, R. Lin, W. Xiao, C. Xuan, H. L. Xin, D. Wang, *J. Mater. Chem. A* **2016**, *4*, 5678–5684.
[29] F. Dong, Y. Cai, C. Liu, J. Liu, J. Qiao, *Int. J. Hydrogen Energy* **2018**, *43*, 12661–12670.
[30] K. Preuss, A. M. Siwoniku, C. I. Bucur, M. Titirici, *ChemPlusChem* **2019**, *84*, 457–464.
[31] D.-S. Yang, D. Bhattacharjya, S. Inamdar, J. Park, J.-S. Yu, *J. Am. Chem. Soc.* **2012**, *134*, 16127–16130.
[32] I. Palm, E. Kibena-Põldsepp, U. Mäeorg, J. Kozlova, M. Käärik, A. Kikas, J. Leis, V. Kisand, A. Tamm, K. Tammeveski, *Electrochem. Commun.* **2021**, *125*, 106976.
[33] J. Wang, Z.-X. Wu, L.-L. Han, Y.-Y. Liu, J.-P. Guo, H. L. Xin, D.-L. Wang, *Chin. Chem. Lett.* **2016**, *27*, 597–601.
[34] R. Ma, G. Lin, Y. Zhou, Q. Liu, T. Zhang, G. Shan, M. Yang, J. Wang, *NPJ Comput. Mater.* **2019**, *5*, 78.
[35] Z. Yang, Z. Yao, G. Li, G. Fang, H. Nie, Z. Liu, X. Zhou, X. Chen, S. Huang, *ACS Nano* **2012**, *6*, 205–11.
[36] Z. Lu, G. Chen, S. Siahrostami, Z. Chen, K. Liu, J. Xie, L. Liao, T. Wu, D. Lin, Y. Liu, T. F. Jaramillo, J. K. Nørskov, Y. Cui, *Nat. Catal.* **2018**, *1*, 156–162.
[37] G.-F. Han, F. Li, W. Zou, M. Karamad, J.-P. Jeon, S.-W. Kim, S.-J. Kim, Y. Bu, Z. Fu, Y. Lu, S. Siahrostami, J.-B. Baek, *Nat. Commun.* **2020**, *11*, 2209.
[38] Y. J. Sa, J. H. Kim, S. H. Joo, *Angew. Chem. Int. Ed.* **2019**, *58*, 1100–1105.
[39] G. V. Fortunato, E. Pizzutilo, E. S. F. Cardoso, M. R. V. Lanza, I. Katsounaros, S. J. Freakley, K. J. J. Mayrhofer, G. Maia, M. Ledendecker, *J. Catal.* **2020**, *389*, 400–408.
[40] D. K. James, J. M. Tour, *Acc. Chem. Res.* **2013**, *46*, 2307–18.
[41] L. Ma, J. Wang, F. Ding, *ChemPhysChem* **2013**, *14*, 47–54.
[42] A. L. Higginbotham, D. V Kosynkin, A. Sinitskii, Z. Sun, J. M. Tour, *ACS Nano* **2010**, *4*, 2059–2069.
[43] T. Wang, Z. Wang, R. V. Salvatierra, E. McHugh, J. M. Tour, *Carbon* **2020**, *158*, 615–623.
[44] Q. Yang, Y. Chen, X. Duan, S. Zhou, Y. Niu, H. Sun, L. Zhi, S. Wang, *Appl. Catal. B* **2020**, *276*, 119146.
[45] S. E. Colthup, N. B. Daly, L. H. Wiberley, *Introduction to Infrared and Raman Spectroscopy*, Academic Press, Inc., **1990**
[46] R. M. Silverstein, F. X. Webster, D. J. Kiemle, *Spectrometric Identification of Organic Compounds*, John Wiley & Sons. Inc., **2005**.
[47] J.-B. Wu, M.-L. Lin, X. Cong, H.-N. Liu, P.-H. Tan, *Chem. Soc. Rev.* **2018**, *47*, 1822–1873.
[48] M. G. Schwab, A. Narita, Y. Hernandez, T. Balandina, K. S. Mali, S. De Feyter, X. Feng, K. Müllen, *J. Am. Chem. Soc.* **2012**, *134*, 18169–18172.
[49] X. Li, T. Li, Q. Zhong, K. Du, H. Li, J. Huang, *Electrochim. Acta* **2014**, *125*, 170–175.
[50] R. Wei, Y. Gu, L. Zou, B. Xi, Y. Zhao, Y. Ma, Y. Qian, S. Xiong, Q. Xu, *Nano Lett.* **2020**, *20*, 7342–7349.
[51] K. Gopalsamy, J. Balamurugan, T. D. Thanh, N. H. Kim, J. H. Lee, *Chem. Eng. J.* **2017**, *312*, 180–190.
[52] Y. Li, J. Yang, J. Huang, Y. Zhou, K. Xu, N. Zhao, X. Cheng, *Carbon* **2017**, *122*, 237–246.
[53] A. N. Abbas, G. Liu, A. Narita, M. Orosco, X. Feng, K. Müllen, C. Zhou, *J. Am. Chem. Soc.* **2014**, *136*, 7555–7558.
[54] M. G. Schwab, A. Narita, S. Osella, Y. Hu, A. Maghsoumi, A. Mavrinsky, W. Pisula, C. Castiglioni, M. Tommasini, D. Beljonne, X. Feng, K. Müllen, *Chem. Asian J.* **2015**, *10*, 2134–2138.
[55] X. Wang, J. Ma, W. Zheng, S. Osella, N. Arisnabarreta, J. Droste, G. Serra, O. Ivasenko, A. Lucotti, D. Beljonne, M. Bonn, X. Liu, M. R. Hansen, M. Tommasini, S. De Feyter, J. Liu, H. I. Wang, X. Feng, *J. Am. Chem. Soc.* **2022**, *144*, 228–235.
[56] D. B. Schuepfer, F. Badaczewski, J. M. Guerra-Castro, D. M. Hofmann, C. Heiliger, B. Smarsly, P. J. Klar, *Carbon* **2020**, *161*, 359–372.
[57] H. W. Kim, M. B. Ross, N. Kornienko, L. Zhang, J. Guo, P. Yang, B. D. McCloskey, *Nat. Catal.* **2018**, *1*, 282–290.
[58] M. S. Dresselhaus, A. Jorio, M. Hofmann, G. Dresselhaus, R. Saito, *Nano Lett.* **2010**, *10*, 751–758.
[59] C. V. Boone, G. Maia, *Electrochim. Acta* **2017**, *247*, 19–29.
[60] C. V. Boone, G. Maia, *Electrochim. Acta* **2019**, *303*, 192–203.
[61] A. S. Souza, L. S. Bezerra, E. S. F. Cardoso, G. V. Fortunato, G. Maia, *J. Mater. Chem. A* **2021**, *9*, 11255–11267.
[62] B. K. Martini, G. Maia, *Electrochim. Acta* **2021**, *8*, 138907.
[63] G. V. Fortunato, E. S. F. Cardoso, B. K. Martini, G. Maia, *ChemElectroChem* **2020**, *7*, 1610–1618.
[64] T. Xiang, Z. Wu, Z. Sun, C. Cheng, W. Wang, Z. Liu, J. Yang, B. Li, *J. Colloid Interface Sci.* **2022**, *610*, 486–494.
[65] G. Zhao, L. Shi, J. Xu, X. Yan, T. S. Zhao, *Int. J. Hydrogen Energy* **2018**, *43*, 1470–1478.
[66] Q. Yang, Z. Xiao, D. Kong, T. Zhang, X. Duan, S. Zhou, Y. Niu, Y. Shen, H. Sun, S. Wang, L. Zhi, *Nano Energy* **2019**, *66*, 104096.
[67] H. Yang, Y. Liu, X. Liu, X. Wang, H. Tian, G. I. N. Waterhouse, P. E. Kruger, S. G. Telfer, S. Ma, *eScience* **2022**, *2*, 227–234.
[68] J. Zhang, Y. Sun, J. Zhu, Z. Gao, S. Li, S. Mu, Y. Huang, *Adv. Sci.* **2018**, *5*, 1801375.
[69] L. Xie, P. Wang, Y. Li, D. Zhang, D. Shang, W. Zheng, Y. Xia, S. Zhan, W. Hu, *Nat. Commun.* **2022**, *13*, 5560.
[70] A. Schürmann, B. Luerßen, D. Mollenhauer, J. Janek, D. Schröder, *Chem. Rev.* **2021**, *121*, 12445–12464.
[71] G. V. Fortunato, E. Pizzutilo, A. M. Mingers, O. Kasian, S. Cherevko, E. S. F. Cardoso, K. J. J. Mayrhofer, G. Maia, M. Ledendecker, *J. Phys. Chem. C* **2018**, *122*, 15878–15885.
[72] S. Zaman, Y. Su, C. Dong, R. Qi, L. Huang, Y. Qin, Y. Huang, F. Li, B. You, W. Guo, Q. Li, S. Ding, B. Yu Xia, *Angew. Chem. Int. Ed.* **2022**, *61*, e202115835.
[73] W. S. Hummers, R. E. Offeman, *J. Am. Chem. Soc.* **1958**, *80*, 1339–1339.
[74] M. Duraivel, S. Nagappan, B. Balamuralitharan, S. Selvam, S. N. Karthick, K. Prabakar, C.-S. Ha, H.-J. Kim, *New J. Chem.* **2018**, *42*, 11093–11101.
[75] C. C. L. McCrory, S. Jung, J. C. Peters, T. F. Jaramillo, *J. Am. Chem. Soc.* **2013**, *135*, 16977–16987.
[76] L. Li, C. Tang, Y. Zheng, B. Xia, X. Zhou, H. Xu, S. Qiao, *Adv. Energy Mater.* **2020**, *10*, 2000789.
[77] Y. Xia, X. Zhao, C. Xia, Z.-Y. Wu, P. Zhu, J. Y. Kim, X. Bai, G. Gao, Y. Hu, J. Zhong, Y. Liu, H. Wang, *Nat. Commun.* **2021**, *12*, 4225.
[78] H. Zhao, X. Shen, Y. Chen, S.-N. Zhang, P. Gao, X. Zhen, X.-H. Li, G. Zhao, *Chem. Commun.* **2019**, *55*, 6173–6176.
[79] L. Han, Y. Sun, S. Li, C. Cheng, C. E. Halbig, P. Feicht, J. L. Hübner, P. Strasser, S. Eigler, *ACS Catal.* **2019**, *9*, 1283–1288.
[80] Y. Sun, S. Li, Z. P. Jovanov, D. Bernsmeier, H. Wang, B. Paul, X. Wang, S. Kühl, P. Strasser, *ChemSusChem* **2018**, *11*, 3388–3395.
[81] M. H. M. T. Assumpção, R. F. B. De Souza, D. C. Rascio, J. C. M. Silva, M. L. Calegaro, I. Gaubeur, T. R. L. C. Paixão, P. Hammer, M. R. V. Lanza, M. C. Santos, *Carbon* **2011**, *49*, 2842–2851.

Manuscript received: September 28, 2023
Revised manuscript received: October 31, 2023
Version of record online: ■■, ■■

RESEARCH ARTICLE

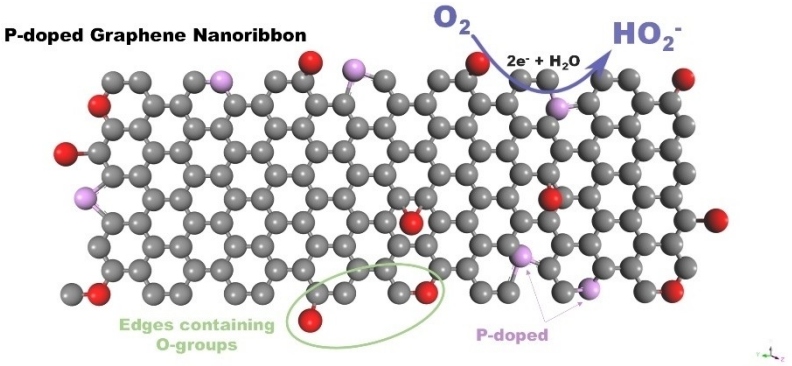

Dr. E. S. F. Cardoso, Dr. G. V. Fortunato, Dr. C. D. Rodrigues, F. E. B Júnior, Prof. Dr. M. Ledendecker, Prof. Dr. M. R. V. Lanza, Prof. Dr. G. Maia**

1 – 15

Impacts of Graphene Nanoribbon Production Methods on Oxygen-Reduction Electrocatalysis in Different Environments

Oxygen-reduction electrocatalysis: The study seeks to unravel the intricate interplay between edge defects, oxygenated groups inherited from the multi-walled carbon nanotubes (MWCNTs) opening process, and their collective influence on the doping process and electrocatalytic properties of graphene nanoribbons (GNRs). We highlight the critical role played by the choice of MWCNT opening methods, which significantly impact GNR characteristics, subsequently influencing ORR performance and H_2O_2 selectivity.